

# Nuclear spirals in the inner Milky Way

Matthew G. L. Ridley,<sup>1</sup>★† Mattia C. Sormani,<sup>2</sup>† Robin G. Treß,<sup>2</sup> John Magorrian<sup>1</sup>  
and Ralf S. Klessen<sup>2,3</sup>

<sup>1</sup>*Rudolf Peierls Centre for Theoretical Physics, 1 Keble Road, Oxford OX1 3NP, UK*

<sup>2</sup>*Zentrum für Astronomie, Institut für theoretische Astrophysik, Universität Heidelberg, Albert-Ueberle-Str. 2, D-69120 Heidelberg, Germany*

<sup>3</sup>*Interdisziplinäres Zentrum für Wissenschaftliches Rechnen, Universität Heidelberg, Im Neuenheimer Feld 205, D-69120 Heidelberg, Germany*

Accepted 2017 April 18. Received 2017 April 12; in original form 2017 February 16

## ABSTRACT

We use hydrodynamical simulations to construct a new coherent picture for the gas flow in the Central Molecular Zone (CMZ), the region of our Galaxy within  $R \lesssim 500$  pc. We relate connected structures observed in  $(l, b, v)$  data cubes of molecular tracers to nuclear spiral arms. These arise naturally in hydrodynamical simulations of barred galaxies, and are similar to those that can be seen in external galaxies such as NGC 4303 or NGC 1097. We discuss a face-on view of the CMZ, including the positions of several prominent molecular clouds, such as Sgr B2, the 20 and 50 km s<sup>−1</sup> clouds, the polar arc, Bania Clump 2 and Sgr C. Our model is also consistent with the larger scale gas flow, up to  $R \simeq 3$  kpc, thus providing a consistent picture of the entire Galactic bar region.

**Key words:** ISM: kinematics and dynamics – galaxies: kinematics and dynamics.

## 1 INTRODUCTION

Since the earliest radio surveys, it has been known that the interstellar medium (ISM) in the Central Molecular Zone (CMZ), the innermost 500 pc of the Milky Way (MW), has a particularly rich and complex structure. The kinematics show significant departures from circular motion, the molecular gas is strongly concentrated within the central degree and the emission is highly asymmetric about the Galactic Centre (GC; e.g. Bally et al. 1988). This region contains some 10 per cent of the total molecular gas of the MW ( $\sim 10^7 M_\odot$ ; Ferrière, Gillard & Jean 2007), and the physical conditions within the CMZ are far more extreme than in the solar neighbourhood and outer regions of the Galaxy. Despite the extremely high column densities and pressures, star formation in the CMZ seems to be suppressed by at least an order of magnitude compared to what is predicted by our current understanding of star formation (e.g. Kennicutt 1998; Longmore et al. 2013a; Kruijssen et al. 2014; Battersby et al. 2016). A proper understanding of the structure and dynamics of gas in the CMZ may help reconcile this contradiction, and give us insight into the mechanics of star formation.

High-resolution molecular line studies of the CMZ have revealed coherent features spanning the width of the  $(l, b, v)$  data cubes in several different species, including CO, CS, NH<sub>3</sub> and HNC (Nagayama et al. 2007; Oka et al. 2007; Henshaw et al. 2016a). The origin of these features has been of interest for several decades,

and proposed explanations include two spiral arms (Sofue 1995; Sawada et al. 2004), a twisted elliptical orbit (Molinari et al. 2011) or an open stream (Kruijssen, Dale & Longmore 2015).

The dynamics of gas in the CMZ are an important topic in itself. Since it is now well established that the MW contains a bar, as confirmed by direct photometric evidence (Blitz & Spergel 1991), it is clear that the dynamics must be understood in the context of gas flowing in a barred potential. In the interpretation of Binney et al. (1991), later refined by Sormani, Binney & Magorrian (2015a) (hereafter *SBM15a*; see also Jenkins & Binney 1994; Rodríguez-Fernández & Combes 2008; Li et al. 2016), gas in the CMZ follows  $x_2$  orbits. These are a family of closed orbits weakly elongated in the direction perpendicular to the bar (Contopoulos & Papayannopoulos 1980). Hence, the CMZ is sometimes referred to as the  $x_2$  disc. The CMZ is fed gas by shocks, which efficiently bring material inwards on to the  $x_2$  orbits from the outer parts ( $R \simeq 2\text{--}3$  kpc).

Our goal in this paper is to demonstrate that the distribution and kinematics of gas in the CMZ can be well modelled by an elongated disc of gas containing two nuclear spiral arms. Nuclear spirals are commonly observed in external barred spiral galaxies (e.g. Schinnerer et al. 2002; Martini et al. 2003a,b; Kuno et al. 2008; van de Ven & Fathi 2010); see Fig. 1 for a striking example. It would therefore be natural to also find them in the centre of our Galaxy. They arise commonly in hydrodynamic simulations in barred potentials (e.g. Ann & Thakur 2005; Li, Shen & Kim 2015); thus, they are automatically consistent with the large-scale flow in and around the bar. If indeed nuclear spirals are present in the centre of the MW, the density enhancement along the spiral arms would result in ridges of emission spanning the width of the CMZ similar to those observed in the  $(l, b, v)$  data cubes. The compression

\* E-mail: [matthew.ridley@physics.ox.ac.uk](mailto:matthew.ridley@physics.ox.ac.uk)

† These two authors contributed equally to this paper.

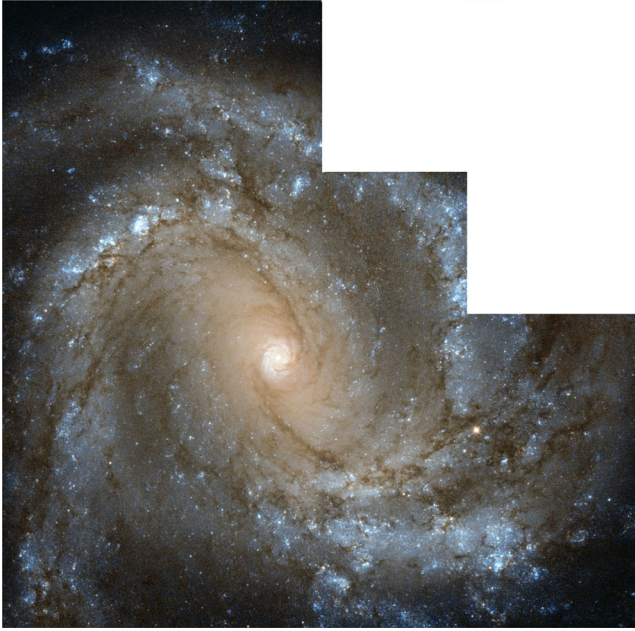


**Figure 1.** An image of the barred spiral galaxy NGC 4303, also known as Messier 61, captured by the *Hubble Space Telescope* Wide Field Camera 2. Nuclear spirals fed by straight dust lanes are clearly visible in the core. Credit: ESA/Hubble and NASA. Acknowledgements: G. Chapdelaine, L. Limatola and R. Gendler; available at [s://www.spacetelescope.org/images/potw1324a/](http://www.spacetelescope.org/images/potw1324a/).

produced by the spiral shocks would provide a natural mechanism for the formation of complex molecular species.

The presence of nuclear spiral arms at the centre of the MW has been discussed for some time. Sofue (1995) used a purely kinematic spiral arm model to deconvolve the  $(l, v)$  distribution of emission in the CMZ to produce a face-on map. Sawada et al. (2004) compared emission and absorption maps to derive distances of clouds along lines of sight without the use of kinematic models, and the resulting face-on map was consistent with the presence of two arms of gas in the central region. However, neither of these was a dynamical model derived from physical principles. Our aim here is to improve on previous work by producing a fully dynamic model of the CMZ consistent with the gas flow in the entire central region of the Galaxy. As we describe below, our picture differs in several significant ways from previous works and corrects some inconsistencies of the spiral arm interpretation of Sofue (1995) and Sawada et al. (2004), as discussed in Henshaw et al. (2016a).

This paper is structured as follows. In Section 2, we discuss the data used in this paper and highlight particular features of interest. In Section 3, we describe the numerical scheme and the potential used to run the hydrodynamical simulation. The results of the model are described in Section 4, and we discuss the successes and shortcomings of the model in Section 5. Finally, in Section 6, we summarize our conclusions.

## 2 DATA

Here we briefly describe some characteristics of the observations. This section should serve as a reference for the remainder of this paper.

We focus on  $\text{NH}_3$  (1,1) emission in the region  $-1^\circ \leq l \leq 3.5^\circ$ , using data from the  $\text{H}_2\text{O}$  Southern Galactic Plane Survey (HOPS; Walsh et al. 2011; Purcell et al. 2012). The data have a spatial

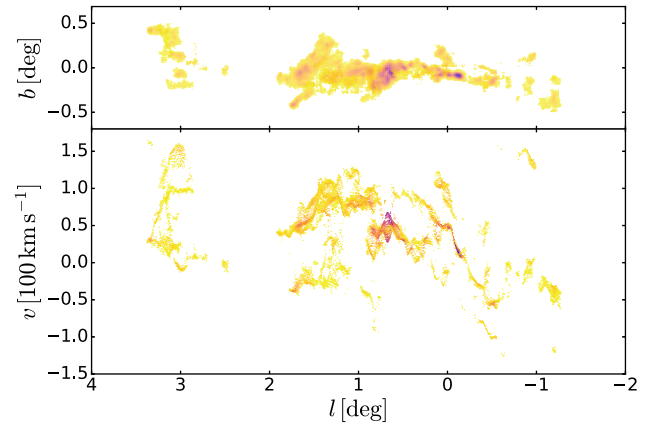


**Figure 2.**  $\text{NH}_3$  (1–1) data from the HOPS survey (Purcell et al. 2012), fitted with the *SCOUSE* algorithm (Henshaw et al. 2016a). Top panel: the spatial distribution of emission in  $(l, b)$ . Bottom panel: the position velocity distribution in  $(l, v)$ . Each point represents a spectral component as determined by the *SCOUSE* algorithm, coloured by brightness temperature (arbitrary units).

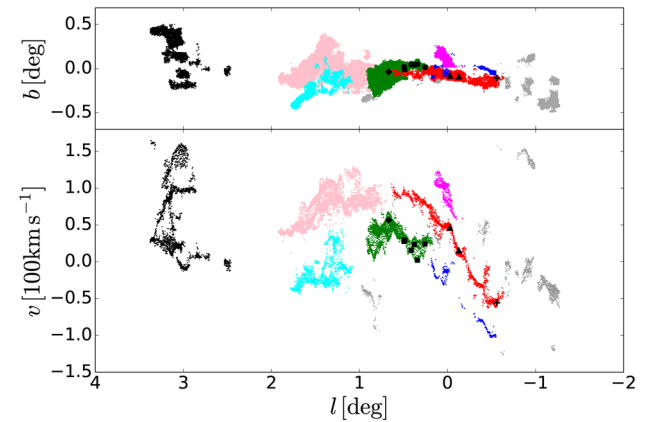


**Figure 3.** The data of Fig. 2, with features of interest highlighted in various colours. Blue points: Arm I. Red points: Arm II. Magenta points: Arm III, also known as the ‘polar arc’. Green points and black diamond: Sgr B2 cloud complex and the dust ridge. Pink points: 1:3 cloud complex. Black points: Clump 2 of Stark & Bania (1986). Cyan points: Cloud complex M of Rodriguez-Fernandez et al. (2006). Black triangles: the 20 and 50  $\text{km s}^{-1}$  clouds. Black plus: Sgr C. Black squares: from the left- to right-hand side, dust ridge clouds B–F and G0.253+0.016, also known as ‘the Brick’.

resolution of  $\sim 60$  arcsec and a spectral resolution of  $2 \text{ km s}^{-1}$ , and have been fitted using *SCOUSE* (Semi-automated multi-COMponent Universal Spectral-line fitting Engine<sup>1</sup>; Henshaw et al. 2016a). These data and the fits are discussed in detail in Longmore et al. (2017).

Although  $\text{NH}_3$  shows some signs of self-absorption in the CMZ, the distribution and kinematics of emission show the same large-scale features as observed in CO (Rodriguez-Fernandez et al. 2006), HNC (Henshaw et al. 2016a) and  $\text{CII}$  (Langer et al. 2017). In this paper, we focus mainly on coherent features in the  $(l, b, v)$  data cube, and not on the precise details of the emission.

Fig. 2 shows the  $(l, v)$  and  $(l, b)$  projections of the *SCOUSE* fits to the data. We note several structures of particular interest, highlighted in Fig. 3:

<sup>1</sup> <https://github.com/jdhenshaw/SCOUSE>

(i) Blue points: Arm I, an extended ridge of emission running from  $l = -0^\circ.7$ ,  $v = 100 \text{ km s}^{-1}$  to  $l = 0^\circ.7$ ,  $v = -50 \text{ km s}^{-1}$ .

(ii) Red points: Arm II, another ridge of emission running parallel to Arm I from  $l = -0^\circ.7$ ,  $v = 70 \text{ km s}^{-1}$  to  $l = 0^\circ.7$ ,  $v = -150 \text{ km s}^{-1}$ . Sofue (1995) identified Arms I and II as two spiral arms within the CMZ; however, Kruijsen et al. (2015) proposed that they are the projection of gas clouds on an open ballistic orbit.

(iii) Magenta points: Arm III, also known as the ‘polar arc’. A high-velocity feature at a large inclination, suggested as a continuation of Arm II by Sofue (1995).

(iv) Green points: Sgr B2 cloud complex and the dust ridge. The Sgr B2 cloud is a well-studied molecular cloud complex around  $(l, b, v) \simeq (0^\circ.7, 0^\circ.1, 10\text{--}70 \text{ km s}^{-1})$ . An unusually high number of independent velocity components are present at each  $(l, b)$  pixel (Henshaw et al. 2016a), and the velocity dispersions are also unusually broad. Suggested explanations for this complex velocity structure include a shell-like arrangement produced by supernovae or the result of a collision between two molecular clouds (e.g. Henshaw et al. 2016a, and references therein). Between Sgr B2 and G0.253+0.016 (the ‘Brick’, rightmost black square) lies a prominent ridge of dust emission containing several molecular clouds. See section 5.1 for a more in-depth discussion.

(v) Pink points: 1:3 cloud complex, a huge molecular cloud structure suggested by Rodriguez-Fernandez et al. (2006) as the site of accretion on to the CMZ.

(vi) Black points: Clump 2, a molecular cloud complex at  $(l, b, v) \simeq (3^\circ, 0^\circ.2, 20\text{--}150 \text{ km s}^{-1})$ . Stark & Bania (1986) suggested that this is the signature of a dust lane or spiral arm due to the complex internal velocity structure.

(vii) Cyan points: Cloud M of Rodriguez-Fernandez et al. (2006), possibly associated with the far side dust lane.

Also shown in the same figure are locations of some prominent molecular clouds. The black triangles are the 20 and  $50 \text{ km s}^{-1}$  clouds, two bright clouds located near to Sgr A\* in projection, believed to be connected to Arm II. The black plus is Sgr C, a star-forming molecular cloud complex at the tip of Arm II, with multiple line-of-sight velocity components. For a more complete discussion, see, for example, Rodriguez-Fernandez et al. (2006) and Henshaw et al. (2016a).

### 3 METHODS

#### 3.1 Numerical scheme

We use the same numerical scheme as in SBM15a and Sormani, Binney & Magorrian (2015b, 2015c). Here we briefly summarize the main points, and refer the reader to the above references for further details.

In our simulations, we assume that the gas is a two-dimensional (2D) inviscid isothermal fluid governed by the Euler equations. The gas is non-self-gravitating and flows in an externally imposed barred potential that rotates with a constant pattern speed  $\Omega_p$ . The potential is described in detail in Section 3.2.

The CMZ has a thickness of 15–30 pc and a radius of  $\sim 200 \text{ pc}$  (Ferrière et al. 2007). As the vertical extent of the gas is so much smaller than the radial extent, our 2D model should be able to capture the important points of the gas flow.

An additional term is introduced in the continuity equation to implement the recycling law of Athanassoula (1992). The recycling law was originally meant to take into account the effects of star formation and stellar mass-loss in a simple way. In practice, the

only effect of the recycling law is to prevent too much gas from accumulating in the very centre and to replace gas lost at the boundary due to the outflow boundary conditions. It does not affect the morphology of the results, so our results do not change if we disable the recycling law. The dynamical equations in an inertial frame are

$$\begin{aligned}\partial_t \rho + \nabla \cdot (\rho \mathbf{v}) &= \alpha_r (\rho_0^2 - \rho^2), \\ \partial_t \mathbf{v} + (\mathbf{v} \cdot \nabla) \mathbf{v} &= -\frac{\nabla P}{\rho} - \nabla \Phi, \\ P &= c_s^2 \rho,\end{aligned}\tag{1}$$

where  $\rho$  is the surface density of the gas,  $P$  is the pressure,  $\Phi$  is the gravitational potential,  $\mathbf{v}$  is the velocity,  $c_s$  is the sound speed,  $\alpha_r$  is a constant representing the efficiency of the recycling law and  $\rho_0$  is the initial surface density. We adopt recycling efficiency  $\alpha_r = 0.3 \text{ M}_\odot \text{ pc}^{-2} \text{ Gyr}^{-1}$  and initial density  $\rho_0 = 1 \text{ M}_\odot \text{ pc}^{-2}$  (Athanassoula 1992).

In our simulations, the gas is assumed to be isothermal with an effective sound speed of  $c_s = 10 \text{ km s}^{-1}$ . This is a phenomenological sound speed that is meant to take into account the effects of small-scale turbulence (e.g. Roberts 1969; Cowie 1980); the ‘temperature’ in our isothermal assumption is therefore related to the velocity dispersion of clouds rather than a microscopic temperature. The average energy content of the gas, and hence the effective temperature, is assumed to be held constant by an energy balance between heating and cooling processes. The observed velocity dispersion of the ISM seems to support this hypothesis (e.g. Dickey & Lockman 1990; Walter et al. 2008; Leroy et al. 2009). Therefore, any heating due to compression, for example, at a shock, is instantaneously radiated away to restore the initial temperature. SBM15a found that the choice  $c_s \gtrsim 10 \text{ km s}^{-1}$  makes the location of the transition from the  $x_1$  to  $x_2$  families of orbits consistent with observations.

We use a grid-based, Eulerian code based on the second-order flux-splitting scheme developed by van Albada, van Leer & Roberts (1982) and later used by Athanassoula (1992), Weiner & Sellwood (1999) and others to study gas dynamics in barred potentials.

Our grid is  $1750 \times 1750$  on a side. The resolution is  $dx = 5 \text{ pc}$ , so the total simulated area is a square with side 8.75 kpc. We start with gas in equilibrium on circular orbits in an axisymmetrized potential and turn on the non-axisymmetric part of the potential gradually during the first 150 Myr to avoid transients. We use outflow boundary conditions: Gas can freely escape the simulated region, after which it is lost forever. The potential well is sufficiently deep, however, to prevent excessive quantities of material from escaping.

To project material to the  $(l, v)$  plane, we assume an angle  $\phi = 20^\circ$  between the Sun–GC line and the bar major axis (the  $x$ -axis of the simulation), consistent with current estimates (e.g. Bland-Hawthorn & Gerhard 2016), and a Sun–GC distance of  $R_0 = 8 \text{ kpc}$ .

#### 3.2 The potential

We use a realistic MW potential that is the sum of four components: bar, bulge, disc and halo. As a starting point, we use the best-fitting potential of McMillan (2017). This is an axisymmetric model, and therefore cannot accurately represent the central region of the Galaxy, which is dominated by a rotating stellar bar. As we focus on this region, and in particular on the effects of the bar, we perform the following modifications:

(i) We add a barred component. This is chosen such that its quadrupole fits the best-fitting quadrupole in Sormani et al. (2015c).

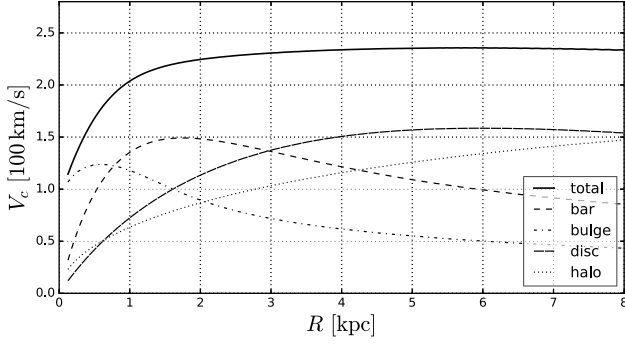


**Figure 4.** The full curve shows the circular velocity curve for the potential used in this paper. The separate contributions from bulge, disc and halo are shown with dot-dashed, dashed and dotted lines, respectively.

(ii) We modify the inner bulge density profile to make it more centrally concentrated, so that the potential has an inner Lindblad resonance (ILR) that is required for the  $x_2$  orbit family to exist as these are believed to provide the backbone for the CMZ.

(iii) We adjust the parameters of the other components to compensate for the introduction of the barred component. This means that we slightly decrease the mass of the disc and the halo in order to compensate for the extra mass introduced by the bar, in such a way that the circular velocity at the Sun position remains approximately constant.

We can expand the potential in the plane of the Galaxy in multipoles as follows:

$$\Phi(R, \phi) = \Phi_0(R) + \sum_{m=1}^{\infty} \Phi_m(R) \cos(m\phi + \phi_m), \quad (2)$$

where  $\phi_m$  are constants and  $\{R, \phi, z\}$  denote planar polar coordinates.

Fig. 4 shows the circular velocity curve of the potential and the contributions from each component separately. Note that our definition of ‘circular velocity curve’ is based on the axisymmetric part of the potential:

$$V_c(R) \equiv \sqrt{R \frac{d\Phi_0}{dR}}. \quad (3)$$

Since the gas undergoes strong non-circular motions in the region dominated by the bar, which, for our Galaxy, corresponds approximately to the region within Galactocentric radius  $R = 3$  kpc (e.g. Binney & Merrifield 1998), the ‘circular velocity speed’ can be significantly different from the speed of the gas obtained in simulations, or observed in the Galaxy, at the same radii (e.g. Binney et al. 1991; SBM15a).

Fig. 5 shows the quadrupole and the octupole of the potential used in this paper. These are generated by the bar, which is the only non-axisymmetric component in our potential.

The details of each component of the potential are as follows.

**Bulge:** This component is generated by the following density distribution:

$$\rho_b = \frac{\rho_{b0}}{(a/a_0)^\alpha} \exp[-(a/a_{\text{cut}})^2], \quad (4)$$

where

$$a = \sqrt{x^2 + y^2 + \frac{z^2}{q_b^2}}. \quad (5)$$

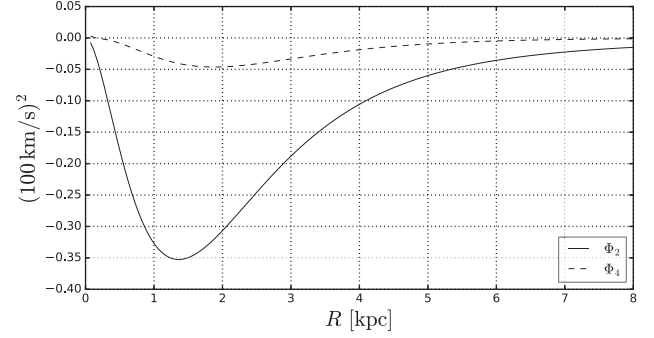


**Figure 5.** The quadrupole  $\Phi_2$  and octupole  $\Phi_4$  of the potential used in this paper.

We use the following values for the parameters:  $\alpha = 1.7$ ,  $\rho_{b0} = 0.8 M_\odot \text{pc}^{-3}$ ,  $a_{\text{cut}} = 1.0$  kpc,  $q_b = 0.5$ , and without loss of generality, we arbitrarily set  $a_0 = 1.0$  kpc. The value  $\alpha = 1.7$  for the inner slope ( $R \lesssim 500$  pc) of the density distribution is consistent with near-infrared photometry (e.g. Bissantz & Gerhard 2002; Launhardt, Zylka & Mezger 2002). We cut the bulge at  $a_{\text{cut}} = 1.0$  kpc as we assume that beyond this radius, the bar dominates over the bulge.

**Bar:** The density of the bar is taken to be

$$\rho_B = \rho_{B0} \exp(-a/a_B), \quad (6)$$

where

$$a = \sqrt{x^2 + \frac{y^2 + z^2}{q_B^2}}, \quad (7)$$

with the following values for the parameters:  $\rho_{B0} = 5 M_\odot \text{pc}^{-3}$ ,  $a_B = 0.75$  kpc and  $q_B = 0.5$ . The bar is also assumed to rotate with a constant pattern speed of  $\Omega_p = 40 \text{ km s}^{-1} \text{kpc}^{-1}$ . This places the ILR at  $R_{\text{ILR}} = 1.2$  kpc. The form of the bar density distribution is chosen to be exponential as infrared (IR) photometry has found the MW bar density profile to be roughly exponential (Wegg & Gerhard 2013). The parameters, including the pattern speed, have been chosen such that the quadrupole of the bar matches the best-fitting quadrupole of Sormani et al. (2015c).

**Disc:** We assume that the disc is the sum of a thick and a thin disc (Gilmore & Reid 1983). The density distribution is

$$\rho_d = \frac{\Sigma_1}{2z_1} \exp\left(-\frac{|z|}{z_1} - \frac{R}{R_{d1}}\right) + \frac{\Sigma_2}{2z_2} \exp\left(-\frac{|z|}{z_2} - \frac{R}{R_{d2}}\right), \quad (8)$$

where  $\Sigma_1 = 850 M_\odot \text{kpc}^{-2}$ ,  $R_{d1} = 2.5$  kpc,  $z_1 = 0.3$  kpc,  $\Sigma_2 = 174 M_\odot \text{kpc}^{-2}$ ,  $R_{d2} = 3.02$  kpc and  $z_2 = 0.9$  kpc. These parameters are slight modifications of the parameters of McMillan (2017).

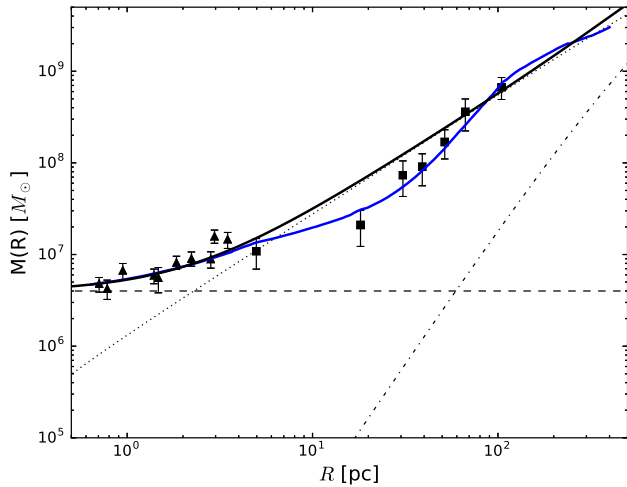
**Halo:** This is a simple Navarro, Frenk & White (1996) profile. The density distribution is

$$\rho_h = \frac{\rho_{h0}}{x(1+x)^2}, \quad (9)$$

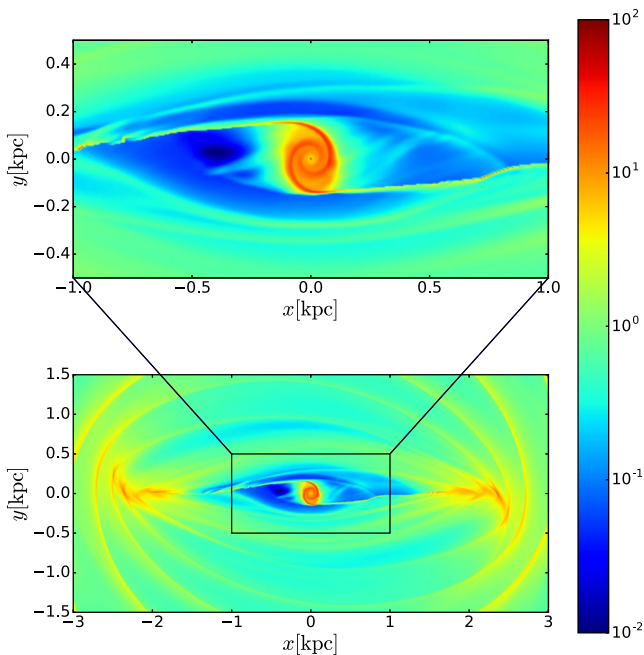
where  $x = r/r_h$ ,  $\rho_{h0} = 0.00811 M_\odot \text{pc}^{-3}$  and  $r_h = 19.6$  kpc. This is a slight modification of the best-fitting model of McMillan (2017).

Fig. 6 compares our stellar mass model of the central region of the MW with results of Launhardt et al. (2002) derived from IR photometry. We find that our model agrees well with the data. We do not explicitly include the potential due to the central black hole Sgr A\* in our simulations as it has no effect on the gas flow at the scales we consider here.





**Figure 6.** Enclosed mass within spheres of radius  $R$  for our model, compared to dynamic and photometric estimates for the MW. Dashed line: a central black hole of mass  $4 \times 10^6 M_\odot$ . Dotted line: the bulge. Dash-dotted line: the bar. Solid black line: the sum of all three components. Solid triangles: McGinn et al. (1989). Solid squares: Lindqvist, Habing & Winnberg (1992). Solid blue line: the total enclosed mass from Launhardt et al. (2002); see their fig. 14.



**Figure 7.** Bottom panel: the fluid density of the simulation at 280 Myr, after the flow has reached an approximate steady state. Top panel: a closer view of the central region of the simulation. The colour bar is in units of  $M_\odot \text{pc}^{-2}$ .

## 4 GAS DYNAMICS

### 4.1 Large-scale gas flow

Fig. 7 shows the surface density of the hydro simulation at  $t = 280$  Myr. At this time, the gas flow has reached an approximate steady state. The large-scale (approximately a few kpc) gas flow in and around the bar can be described along the lines detailed in SBM15a and Sormani et al. (2015b,c). We briefly recap the main points here, and refer the reader to the above papers for

further details. Far from the centre, outside  $R \sim 1$  kpc, the gas closely follows closed orbits belonging to the  $x_1$  family, which are highly elongated along the major axis of the bar. While approximately following the  $x_1$  orbits, the gas also slowly drifts inwards until, close to the ILR, the ‘cusped’  $x_1$  orbit is reached. At this point, the gas cannot continue to follow the  $x_1$  orbits because they become self-intersecting. The gas piles up at these cusps, and two almost straight shocks form from gas plunging almost radially from the tips of the  $x_1$  orbits towards the CMZ, where it settles on the less extended, more circular  $x_2$  orbits, forming a central disc.

Thus, closed ballistic orbits are the key to understand the gas flow. Note that the word *closed* (as opposed to *open* ballistic orbits) is crucial here. As noted by Binney et al. (1991), when clouds of gas are released into a potential, the clouds will, in general, shear and eventually settle on to closed orbits, as collisions tend to dissipate the excess energy of large excursions around these closed orbits (most open ballistic orbits can be interpreted as excursions around a ‘parent’ closed ballistic orbit, which are  $x_1$  and  $x_2$  orbits in this case). Thus, while pressure forces are important in collimating gas on to closed orbits, they are much less significant during the long periods in which the gas drifts from one closed orbit to the next. In this latter regime, pressure forces are, however, responsible for the librations that generate the spiral arms as kinematic density waves (see Sormani et al. 2015b, and the next section). This is why, away from transition between different orbit families, closed ballistic orbits provide a good approximation to the gas flow despite the presence of the pressure term in the equations of motion (see fig. 5 in SBM15a).

Many important observational features in the region  $|l| \leq 30^\circ$  (e.g. the 3-kpc arm, the  $135 \text{ km s}^{-1}$  arm, the terminal velocity curve and others; see, for example, Fux 1999; Sormani et al. 2015c; Li et al. 2016), which approximately corresponds to  $R \lesssim 3$  kpc, can be explained by a gas flow such as the one described above. The main point of interest for this paper is that the CMZ is embedded in a consistent gas flow that can reproduce features of the whole barred region, and not just of the CMZ. Accretion of gas on to the CMZ is obtained automatically as a result of the simulation.

A hydrodynamic simulation such as the one described above can become unstable when one reaches a sufficiently high resolution. This is commonly observed in simulations of this type (e.g. SBM15a; Kim et al. 2012), and is believed to be a real physical phenomenon, dubbed the ‘wobble instability’ (Wada & Koda 2004; Kim, Kim & Kim 2014). We will discuss this further in Section 5.2. None the less, averaged over time, the large-scale features of the flow remain approximately constant.

### 4.2 Nuclear spirals

Nuclear spirals are evident in the inner region ( $R \lesssim 500$  pc) in Fig. 7, with the outer end of each spiral arm connected to the inner end of each shock. We propose below that some of the streams observed in the data are associated with such nuclear spirals. The presence of nuclear spirals is not in contradiction with the fact that gas approximately follows  $x_2$  orbits. Indeed, the gas does follow  $x_2$  orbits well, but not *exactly*: Tiny *librations* around the  $x_2$  orbits ‘interfere constructively’ and generate the spiral arms as kinematic density waves, by exactly the same mechanism described in Sormani et al. (2015b, see their figs 10–12). The only difference is that here librations are around  $x_2$  orbits rather than  $x_1$  orbits, as in Sormani et al. (2015b).

It follows from the nature of the spiral arms as kinematic density waves that gas does not flow *along* the spiral, but has a

significant component of the velocity perpendicular to it. In other words, streamlines cross the spiral arms at an angle, and a fluid element that is instantaneously on a spiral arm moves away from it at a later time. In our simulation, gas usually gets compressed when entering the spiral arm and decompressed when leaving it again. However, in the real ISM, if material is compressed in the spiral arm to the point that a cloudlet that can be considered as a separate entity is formed, this cloudlet will continue to move along the streamline, leaving the spiral arm. Therefore, it is possible for an overdense cloudlet to leave the spiral, despite larger scale decompressions, and remain recognizable as an individual entity. Even in our ‘smooth’ simulations, we have observed this behaviour: Material flowing down the shock and entering the inner spiral can fragment as a consequence of the wiggle instability (see Section 5.2). These fragments are observed to move out from the spiral, in the manner that droplets of water leave the surface of a spinning football. These fragments/cloudlets will continue on approximate ballistic orbits around the CMZ, until colliding with material that has been falling down the shock near the point where it feeds the other spiral arm.

The precise morphology of the nuclear disc and spiral arms is affected by the resolution and sound speed of the simulation (SBM15a). This dependence is complex. Both the resolution and the sound speed affect the location at which the shocks form, and hence the location at which gas is fed on to the CMZ. They also affect the dynamics within the CMZ, such as the stability of the flow (see Section 5.2). We leave a full discussion to later work, and set the resolution (5pc, of the order of the size of a single molecular cloud) and the sound speed to reasonable values in our model in order to focus on discussing how nuclear spirals, if indeed present in the MW, would appear in observations and affect the dynamics of gas within the CMZ.

## 5 DISCUSSION

### 5.1 Interpretation of $(l, v)$ features and face-on map of the CMZ

Using our model of the gas flow, we can understand the features previously identified in the data. Fig. 8 shows a close-up view of the central region of the simulation, with several features of the flow highlighted. In red and blue are the outer parts of the near-side and far-side spiral arms, respectively, and in green is the positive-latitude shock connecting the tip of the cusped  $x_1$  orbit to the  $x_2$  disc. The bottom panel shows the projection of these features in the  $(l, v)$  plane. Also shown are the  $\text{NH}_3$  data for comparison.

#### 5.1.1 Arms I and II

In the longitude–velocity plane, the two spiral arms produce two parallel ridges of emission reaching from positive latitude and velocity to negative latitude and velocity (red and blue in the bottom panel of Fig. 8). Moving outwards-in along the red (blue) arm in the top panel of Fig. 8, the corresponding trace in the bottom panel is from negative (positive) longitude and velocities to positive (negative) longitude and velocities. As the tangent point between the line of sight and the spiral arm is approached, approximately where the red and blue colours end in Fig. 8, the direction of movement in the  $(l, v)$  plane is reversed and we go back again towards negative (positive) longitudes.

The two parallel ridges in the bottom panel of Fig. 8 have a similar range in longitude and a similar slope to Arms I and II in Fig. 3.

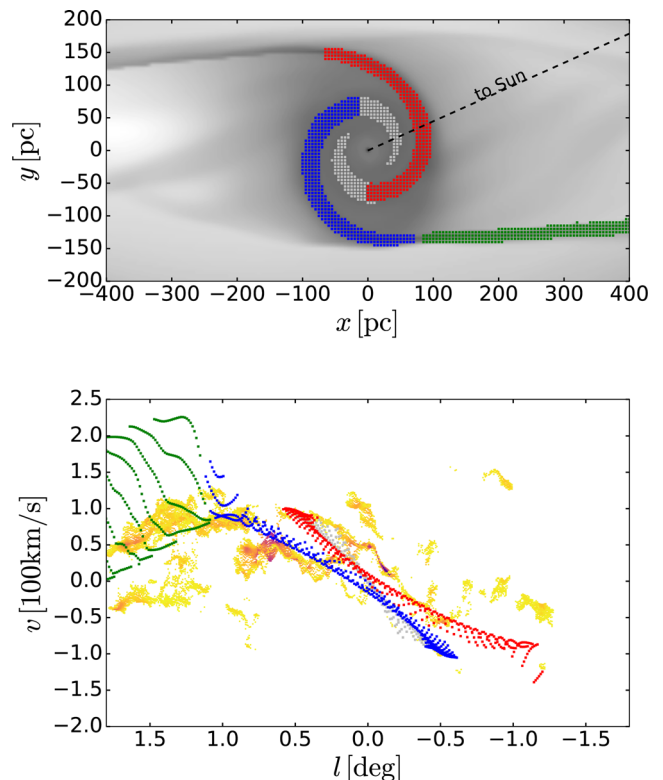


**Figure 8.** Top panel: the near- and far-side nuclear spiral arms and the positive-latitude shock are highlighted in red, blue and green, respectively. The inner regions of both arms are also highlighted in grey. Dashed line: the Sun–GC line for our assumed viewing angle of  $\phi = 20^\circ$ . Bottom panel: projection of the highlighted features to the  $(l, v)$  plane, plotted with the data of Fig. 2.

Thus, we identify Arm II (I) as the projections of the near-side (far-side) nuclear spiral arm. These two features were identified with two spiral arms also in the interpretation of Sofue (1995). However, in the interpretation of this author, the two arms were swapped in the  $(l, v)$  plane: They identified the Arm I (II) as the projections of the near- (far-) side nuclear spiral arm, the opposite of our interpretation. This difference allows us to correct an inconsistency of the spiral arms of Sofue (1995) pointed out by Henshaw et al. (2016a) regarding the placements on the 20 and 50 km s<sup>−1</sup> clouds (see Section 5.4 below).

We interpret Arm III (the ‘Polar Arc’) as a spur of gas extending from Arm II (as proposed in Binney et al. 1991); however, we note that our simplified 2D model cannot explain its position at high inclination.

#### 5.1.2 $l \approx 3$ cloud complexes

Fig. 9 shows a face-on view of the CMZ, together with streamlines of the gas flow. As discussed in Section 4, streamlines do not follow the spiral arms, but go through it at an angle. A dense cloudlet, formed, for example, as a consequence of compression in the arm, can leave the spiral arm and continue its course along a streamline. Such a cloudlet eventually collides with material that has been flowing down the positive-latitude shock, at a position that depends on where it is ejected from the spiral arm. Such collisions would create cloud complexes with complicated spatial and velocity structure.

We have observed this happening in our simulations: The gas fragments due to the wiggle instability, and the fragments tend

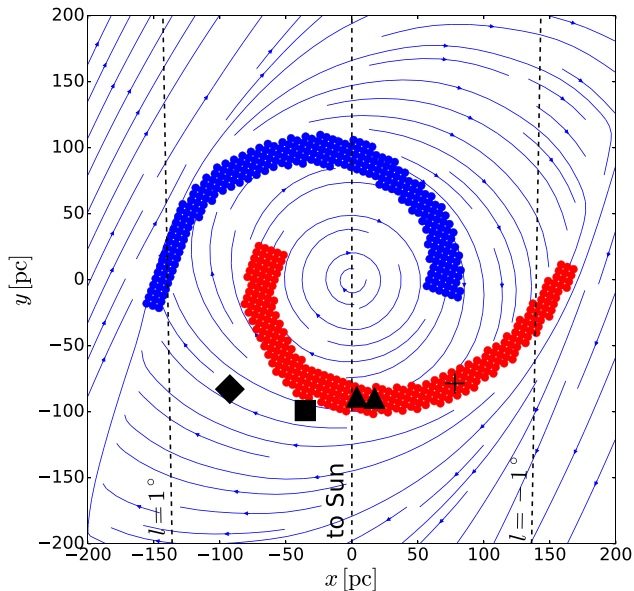


**Figure 9.** A face-on schematic view of the model of the CMZ. The figure has been rotated so that the Sun is at  $(x, y) = (0, -8)$ . The near- and far-side spiral arms are shown in red and blue, respectively. Streamlines of the gas flow are shown. The black symbols denote the locations of prominent molecular clouds, as in Fig. 3. From the left- to right-hand side: Sgr B2 (rotated square), G0.253+0.016, also known as ‘the brick’ (square), the 20 and 50  $\text{km s}^{-1}$  clouds (upward triangles), and Sgr C (plus).

to leave the spiral arms by following the streamlines and collide with material entering the other arm. Similar behaviour is seen, for example, in the simulations of Dobbs et al. (2008) or Smith et al. (2014), who model the dynamics of the ISM and molecular cloud formation during spiral arm passage on large galactic scales. In the real ISM, a cloudlet could form also by other means, for example, as a consequence of becoming quasi-self-gravitating after compression. However, we do not include self-gravity in this paper.

We also expect material to be ejected out of the plane of the CMZ as a consequence of collisions. This could explain why the observations look thicker in latitude on the left and right edges of the CMZ (top panel of Fig. 3), where the areas surrounding Sgr B2 and 1:3 cloud complexes on one side and Sgr C on the other side are suggestive of two ‘lobes’ at the sides of the CMZ. Thus, the blue and pink on one side and the grey on the other side in the top panel of Fig. 3 could be the two sites where the shocks feed the two inner spirals.

Thus, we interpret the 1:3 cloud complex as the result of cloud–cloud collisions between the end of the dust-lane shock and the inner disc, and Sgr B2 as material that has detached from the red arm (discussed further below). In this interpretation, the observed complicated velocity structures and unusually large vertical extent of the gas (see cyan and pink points in the top panel of Fig. 3) are created by collisions (as interpreted also by Bally et al. 2010).

### 5.1.3 Placement of prominent molecular clouds

An understanding of the history of the environment of a star-forming molecular cloud would give insight into the physical processes that can trigger and regulate star formation. Several gas clouds in the CMZ have been identified as the possible progenitors of star clusters (Longmore et al. 2013b); the locations of these prominent cloud complexes within the CMZ are therefore of particular interest be-

cause they represent an excellent opportunity to study star formation in extreme conditions (Kruijssen et al. 2014).

Using the steady-state velocity field of the gas flow, any  $(l, v)$  point can be deprojected to one or more  $(x, y)$  positions: In practice, there will often be two or more points along a line of sight with the same line-of-sight velocity, so additional information is required to map a given point in  $(l, v)$  space to the  $(x, y)$  plane.

The Brick (Lis & Menten 1998; Longmore et al. 2012; Rathborne et al. 2015), and the 20 and 50  $\text{km s}^{-1}$  clouds (Molinari et al. 2011) have been detected in absorption at IR wavelengths, which suggests that they lie in front of the GC. In addition, Reid et al. (2009) measured both the parallax and proper motion of water masers in Sgr B2, placing it at  $130 \pm 6 \text{ pc}$  in front of the GC with  $(\mu_l, \mu_b) = (2.3 \pm 1.0, -1.4 \pm 1.0) \text{ mas yr}^{-1}$ . These data break the degeneracy of our model, allowing us to place these clouds within the CMZ.

Plotted in Fig. 9 are the positions of some prominent molecular clouds in our interpretation. The 20 and 50  $\text{km s}^{-1}$  clouds, with Sgr C, lie along the near-side spiral arm, in front of the GC.

As noted by Kruijssen et al. (2015), the Sgr B2, the dust ridge and the Brick seem to form a continuous structure in  $(l, b, v)$  space. This region of emission (the green points in Fig. 3) is complex, with multiple components, and it is tempting to identify this structure as the continuation of Arm I. However, this would place the clouds behind the GC, while the data suggest the opposite. Therefore, we interpret this region of emission as the superposition of two distinct physical regions in the Galaxy that happen to be at the same location in the  $(l, v)$  projections: Arm I behind the GC, and a spur of material detaching from Arm II on the near side, containing the Brick, dust ridge clouds and Sgr B2.

This is also consistent with the observations that Sgr B2 is host to a high rate of star formation. The compression created by cloud–cloud collisions would provide a natural mechanism for triggering gravitational collapse and star formation.

We should always take these interpretations with a grain of salt. For example, it is also tempting to connect Sgr B2 and the Brick with Arm I, the far-side arm. The presence of the Brick in absorption together with the observed parallax and proper motion of Sgr B2 would go against this interpretation. However, this relies on the assumption that we know the IR emission patterns within the CMZ, and clouds in front of the GC show absorption and clouds behind the GC are obscured. We should bear in mind that while these assumptions are plausible, there is always the possibility that they are incorrect.

### 5.1.4 Summary

To summarize, we interpret the following:

- (i) Arm II (I) as the projections of the near-side (far-side) nuclear spiral arms.
- (ii) Sgr B2, the dust ridge, and the Brick cloud as a spur of material detaching from the red arm, the end of which (Sgr B2) is colliding with shocked material reaching the inner disc.
- (iii) The 1:3 cloud complex on one side and the area surrounding Sgr C on the other side as the two sites where the shocks feed the two spiral arms.
- (iv) The polar arm as a spur of material detaching from the red arm (at a further out location than Sgr B2).
- (v) The 20 and 50  $\text{km s}^{-1}$ , and Sgr C clouds as condensations along the near-side spiral arm.

We remind the reader that the model outlined here is to be seen more as a ‘cartoon’ sketch that provides a framework for interpreting



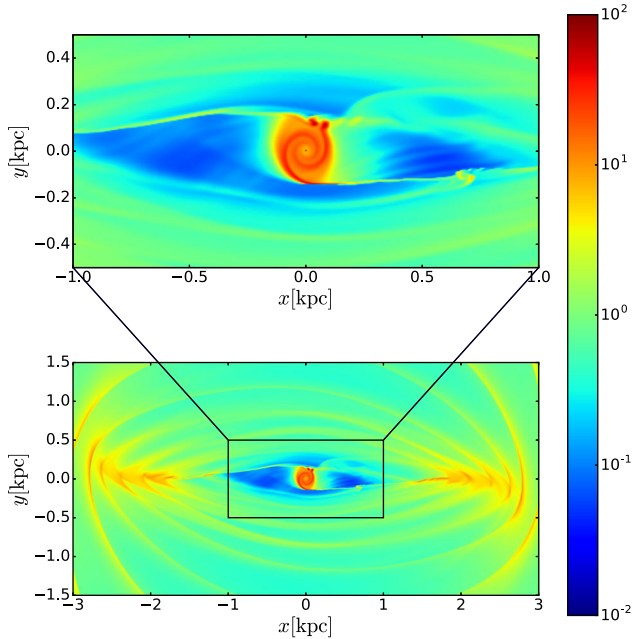


**Figure 10.** Bottom panel: the fluid density of the simulation at the earlier point of 207 Myr. The flow has reached an approximate steady state, but shows several signs of unsteadiness. Top panel: a closer view of the central region of the simulation. The colour bar is in units of  $M_{\odot} \text{pc}^{-2}$ .

the gas flow in the CMZ rather than a detailed fit to all individual observational features. Our interpretation is the result of simulations that were intended to describe the larger-scale flow pattern in the Galactic bar that were not fine-tuned to model the CMZ. So there is certainly room for improvement. We hope that future 3D models that keep track of the chemical evolution of gas flowing in the CMZ will provide further insight.

## 5.2 Signatures of unsteady flow

The gas flow shows a small amount of unsteadiness. This type of instability, where the shocks continuously develop vortices along their length, breaks apart, and reform is commonly observed in simulations of gas flow in barred potentials (Kim et al. 2012; SBM15a; Fragkoudi, Athanassoula & Bosma 2017), and has been dubbed the ‘wiggle’ instability. It does not appear to be a numerical artefact, as it appears in simulations run with many different codes (SBM15a). Kim et al. (2014) used a shearing-box analysis to show that the instability originates from the generation of potential vorticity behind the curved shocks. This potential vorticity is amplified as it passes through successive shocks, leading to an instability that periodically destroys the spiral shocks.

Our model is mostly stable; however, there are a few signatures of the wiggle instability in the flow. Fig. 10 shows the gas density at  $t = 207$  Myr in the simulation. The flow in the inner region shows some signs of unsteadiness. Most noticeably, a bead of material has formed along the positive-latitude shock, and two clumps of material have formed along the near-side spiral arm. The features are highlighted (in black and pink, respectively), in Fig. 11, along with their counterparts in the  $(l, v)$  plane.

The two pink ‘clumps’ are formed as a consequence of the wiggle instability. Dense material belonging to the pink region is seen detaching from the spiral arms and later colliding with material on the blue arm, close to the point where it is fed by the green shock,

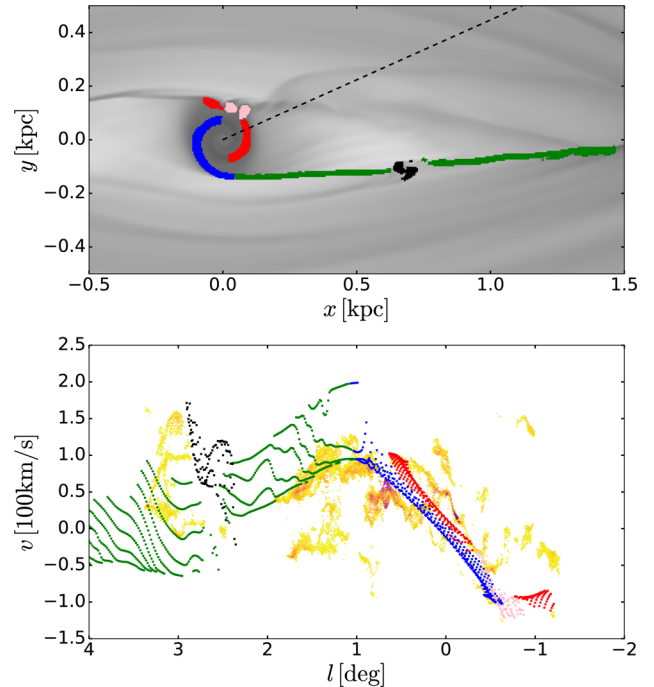


**Figure 11.** The same as Fig. 8, for the earlier point of the simulation with two additional features of the flow highlighted. Black points: a ‘bead’ of material on the positive latitude shock. Pink points: two clumps of material along the near-side spiral arm. Both are signatures of the wiggle instability.

as in our interpretation of the Sgr B2 and 1:3 cloud complexes in Section 5.1.2.

### 5.2.1 Clump 2 cloud complex

It is particularly tempting to associate the signature of the black ‘bead’ along the shock in Fig. 11 with the Clump 2 cloud complex. They are almost coincident in  $(l, v)$  space, and have a similar velocity structure. We therefore interpret the Clump 2 cloud complex as material that is in the process of transitioning from the  $x_1$  to the  $x_2$  orbits, part way down the shock, as originally suggested by Stark & Bania (1986).

The rest of the emission from the shock (in green) covers a broad region of positive velocities with  $l \geq 1.5$ . Therefore, it is natural to ask why we do not see emission covering this region in the MW. In practice, if one performs a simple radiative transfer calculation (assuming that material is optically thin), the two shocks are almost invisible in projection (see, for example, fig. 5 in Sormani et al. 2015c) because a limited amount of fast-moving material is spread over a large area in the  $(l, v)$  plane.

The actual distribution of emission from the shocks will depend on the positions of clouds along the shock and the efficiency of conversion from atomic to molecular gas (SMB15a), and both will be affected by the wiggle instability. As such, it is unsurprising that only a small portion of the  $(l, v)$  region covered by the shock is visible in emission. Sormani et al. (2015c) have suggested that all the vertical features identified in the  $(l, v)$  plane (which include the Clump 2 complex, see their fig. 3) are different portions of the two shocks. Simulations including live chemical networks to test this hypothesis are in preparation.



### 5.2.2 Asymmetry and star formation

The wiggle instability might be responsible for at least three other important facts related to the CMZ:

(i) Approximately, three-quarters of the molecular emission from  $|l| \lesssim 4^\circ$  come from positive longitudes (e.g. Bally et al. 1988; Burton, Elmegreen & Genzel 1992). In particular, we note that Arm II is far weaker in emission than Arm I, and there appears to be no counterpart to the Sgr B2 and 1°3 cloud complexes at negative latitudes. The cause of this asymmetry is a long-standing puzzle. The asymmetry is too big to be attributed solely to a perspective effect from an inclined bar (Jenkins & Binney 1994). SBM15a have argued that, at least in part, the marked asymmetry of molecular emission in the GC can be explained by an unsteady flow. Wiggle instabilities in the shocked flow feeding the CMZ will give rise to unsteady conversion of atomic to molecular gas, so the atomic/molecular ratio on each side of the GC would fluctuate widely. If the conditions in the GC are suitable to produce the wiggle instability, the nuclear spirals will continuously break apart and reform, and the flow of material down the shocks will be intermittent. This provides a natural explanation for the asymmetry: At the current point in time, the near-side spiral arm is in a more intact state than the far side, and the flow of material down the negative latitude shock is in a quiescent phase opposed to the positive-latitude shock, which is actively feeding the nuclear disc.

(ii) The star formation rate in the CMZ is lower by a factor of  $\simeq 10$  than expected from current theories of star formation. Kruijssen et al. (2014) argue that turbulence is the likely cause for this anomaly (see also Bertram et al. 2015). The wiggle instability may also be an important source of turbulence in the CMZ.

(iii) Henshaw, Longmore & Kruijssen (2016b) recently reported the detection of ‘corrugations’ in a stream of gas within the CMZ, which they identify as gas streaming towards molecular cloud condensations seeded by gravitational instabilities. However, if the spiral shocks are being deformed by the wiggle instability, this would also produce an oscillation in the  $(l, v)$  structure very similar to observations.

### 5.3 3D distribution of gas

Molecular emission from the GC has a non-trivial vertical structure, as can be also seen in the top panel of Fig. 2. In a series of papers, Burton & Liszt (1978), Liszt & Burton (1978) and Liszt & Burton (1980) have argued that the inner region of the Galaxy is tilted, so that gas in the central disc ( $R \lesssim \text{few kpc}$ ) does not lie in the plane  $b = 0$  (see also Heiligman 1987; Ferrière et al. 2007, and section 9.4 of Binney & Merrifield 1998). The main observational evidence for the tilt is as follows:

- (i) In the central disc, emission at positive (negative) longitudes mostly lies at negative (positive) latitudes.
- (ii) Longitude–velocity diagrams obtained by slicing the H I and CO data cubes along a line parallel to  $b = -l \tan 22^\circ$  rather than  $b = 0$  show a much higher degree of symmetry.

Although our model is 2D, we can produce crude  $(l, b)$  maps by modelling the CMZ as a tilted razor thin disc. The orientation of the normal  $\hat{n}$  to the disc can be specified by two angles  $(i, \alpha)$ , which are usual polar angles of a spherical coordinate system whose zenith lies along the GC–Sun line and correspond to the angles with the

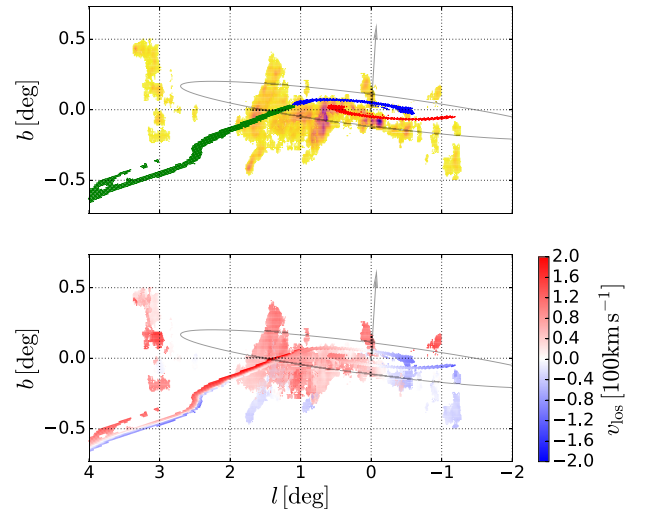


**Figure 12.** A crude 3D model of the CMZ produced by inclining and tilting the simulation as a razor-thin disc. The top panel shows the same features highlighted in Fig. 8. The bottom panel shows the same, but with both data and model coloured by line-of-sight velocity. The grey arrow shows the normal to the disc  $\hat{n}$ , while the grey full line shows the projection of an ellipse elongated perpendicularly to the bar of size  $200 \times 400 \text{ pc}^2$ .

same names in Burton & Liszt (1978).<sup>2</sup>  $i$  corresponds to the usual inclination angle such that  $i = 0^\circ$  and  $90^\circ$ , respectively, represent face-on and edge-on discs, while  $\alpha$  is the angle that the normal to the disc makes with the line  $l = 0$  in the plane of the sky, measured counterclockwise.

Fig. 12 shows the results of this procedure for  $(i, \alpha) = (85.7, -2.5)^\circ$ , which corresponds to an angle of  $\theta = 5^\circ$  between the normal to the disc and the normal to plane of the Galaxy at large. The top panel shows the regions discussed in Section 5.1 and shown in Fig. 8, using the same colour code. The bottom panel shows the same, but coloured by line-of-sight velocity. The angle between the GC–Sun line and the major axis of the bar is  $\phi = 20^\circ$  as before.

(i) Within the region  $-1^\circ \leq l \leq 1^\circ$ , the majority of the emission lines up well along our spiral arms (blue and red). Thus, the tilted model captures the  $(l, b)$  structure of the streams.

(ii) Outside the inner degree, the gas has a far larger vertical extent than would be expected from our simple model. As discussed in Section 5.1, we interpret this region (i.e. the Sgr B2 and 1°3 cloud, green and purple in Fig. 8) as the site of cloud–cloud collisions between material at the innermost tip of the shock and the nuclear disc. These may result in material being thrown out of the plane, producing the kind of structure seen in Fig. 2.

In our model,  $i < 90^\circ$ , which means that the near arm (red) lies at  $b < 0$ , while the far arm (blue) lies at  $b > 0$ . Our value of  $i$  is in agreement with previous estimates given in Burton & Liszt (1978) and Liszt & Burton (1978, 1980).

We have found that models with small negative  $\alpha$  give a qualitatively better fit to the streams, while previous works favoured  $\alpha > 0$ . Indeed, the first observational evidence mentioned above, i.e. the fact that material at positive (negative) latitude is observed

<sup>2</sup> If XYZ are Cartesian right-handed coordinates centred at the GC with the Sun lying on the positive Z-axis and X pointing towards the North Galactic Pole, then

$$\hat{n} = \sin i \cos \alpha \hat{X} + \sin i \sin \alpha \hat{Y} + \cos i \hat{Z}. \quad (10)$$

at positive (negative) longitudes, seems to naively imply that  $\alpha > 0$ . However, Fig. 12 shows that there is another possibility: If most of the emission comes from material in and around the green shock, then one could still obtain the observed apparent tilt even with a small  $\alpha < 0$ . Moreover, the transition point where gas transits from  $x_1$  to  $x_2$  orbits, which is likely to be a locus of bright emission, also lies in the quadrants that give the correct observed tilt in the  $(l, b)$  plane. This reconciles our model with previous estimates. Of course, this is not the only possible explanation. We have assumed that the whole inner region lies on the same plane, but it is also entirely possible that the orientation of the disc changes with radius.

Our discussion is based on purely geometrical considerations. To the best of our knowledge, the dynamical reason for the tilt is at present unknown. Ultimately, real 3D models rather than tilted 2D models are needed to fully understand the vertical structure of the CMZ.

#### 5.4 Comparison with previous work

The presence of spiral arms at the centre of the MW has been discussed for some time. However, ours is the first dynamical model that takes the larger scale Galactic bar into account consistently, and differs from previous models in several significant ways.

The model of Sofue (1995) is purely kinematic. There it was assumed that gas flows parallel to the spiral arm. As we have already emphasized, the gas in our model does not flow *along* the spiral, but rather *across* it, which allows clouds to leave the spirals. This is also a key difference between our model and the open stream model of Kruijssen et al. (2015). In the latter, the observed streams in the  $(l, v)$  plane are produced by gas flowing along a single open ballistic orbit, and therefore one could try to identify a temporal sequence as the gas evolves along the orbit (an hypotheses suggested by Longmore et al. 2013b). In our model, instead, the observed streams are the projection of spiral density waves, i.e. density enhancements, which are caused by librations around  $x_2$  orbits as discussed in Section 4.1. Whether a temporal sequence could be identified is less straightforward in our model, especially on time-scales longer than a fraction of the dynamical time needed to cover an  $x_2$  orbit.

Another difference between ours and the model of Sofue (1995) is that the two arms are swapped in the  $(l, v)$  plane: They identified the near Arm II (I) as the projections of the near-side (far-side) nuclear spiral arm, the opposite of our interpretation.

The spiral arm models of Sofue (1995) and Sawada et al. (2004) were reconsidered by Henshaw et al. (2016a), but it was discounted in favour of the open stream model of Kruijssen et al. (2015). This was primarily because the configuration of arms that was considered placed the 20 and 50 km s<sup>-1</sup> clouds on the far side of the GC, and as these clouds are seen in absorption (Molinari et al. 2011), they are most probably on the near side. The model we present here corrects this inconsistency, as the 20 and 50 km s<sup>-1</sup> clouds are connected to Arm I, which we place on the near side of the CMZ (the red points in Fig. 8).

Kruijssen et al. (2015) have argued that observations suggest that Arm II and the Sgr B2 and I<sup>3</sup>3 cloud complexes are unconnected, separate features (see the red circle in their fig. 2 and the discussion in their section 2.3). In our model, this is indeed the case, as they correspond to projections of physically distinct parts of the gas flow. In contrast, they were connected in the model of Molinari et al. (2011).

Using an unbarred, axisymmetric potential based on the density profile of Launhardt et al. (2002), Kruijssen et al. (2015) showed

that if one assumes that the coherent gas streams in the CMZ all lie along a single ballistic orbit, then an orbit can be found that fits the observed  $(l, b, v)$  distributions of the streams well. Their model fails to explain how gas from the larger scale flow might end up on such an orbit, however. Our model was not originally intended to provide a fit to the CMZ data, but instead was constructed to match the larger scale flow pattern in the Galactic bar. In that sense, it is a ‘by-product’ that it also happens to provide a natural explanation for the origin of the coherent features seen across the CMZ. It automatically accounts for the inflow of shocked gas into the CMZ, and the effect of the non-axisymmetric potential of the bar, both of which are likely to have important consequences on the characteristics of the gas dynamics in the CMZ. We do not assume that the gas streams lie along a single orbit, and indeed find that in our model, this is not the case. For example, according to our model, the 20 and 50 km s<sup>-1</sup> clouds are probably not along the same streamline, but on neighbouring distinct streamlines.

The main weakness of our model is that the projections of the spiral arms are at lower velocities than their observational counterparts. In particular, the near-side arm (red in Fig. 3) would need to be at higher line-of-sight velocities to fully match the observations. However, we note again that our model is not tuned to fit the CMZ. The potential is a relatively simple multicomponent model of the Galaxy, in which the quadrupole was chosen to fit several completely different large-scale features of the Galactic  $(l, v)$  diagram rather than the CMZ (Sormani et al. 2015c). It is thus remarkable how closely the model reproduces the majority of the observed features in the CMZ, although features in our simulation and those in the data do not line up perfectly. This also leaves ample space open for improvement: It is very likely that a better fit can be obtained by fine-tuning the potential and/or making the simulations more sophisticated, for example, making them 3D, adding self-gravity, or moving on from the simple assumption of an isothermal gas by adding heating and cooling sources and keeping track of the chemistry of the ISM.

There are several other factors that may affect gas flow in the CMZ not considered here, primarily magnetic fields and stellar feedback. Crocker et al. (2010) found a lower limit of 50  $\mu$ G for the magnetic field on 400 pc scales near the GC; however, Kruijssen et al. (2014) argued that, assuming equipartition, gas densities in the CMZ are above the critical density at which turbulent pressure dominates over magnetic pressure. They also argue that the observed star formation rate in the CMZ is too low for stellar feedback to overcome turbulent pressure. Therefore, following previous work, we assume that the dominating factor driving gas flow on the scales considered here is the response to the gravitational potential.

## 6 CONCLUSION

In this paper, we have shown that several features present in  $(l, b, v)$  data cubes of molecular emission from the CMZ can be reproduced by nuclear spiral arms arising from gas flow in a barred potential. We have presented a simple hydrodynamical model of isothermal gas moving in an externally imposed barred potential, which was designed to reproduce features of the gas flow on a much larger scale. In the simulation, a central disc of gas on  $x_2$  orbits develops, containing two spiral arms. The disc is connected to the outer regions of the simulation by two shocks.

The model provides a very natural explanation for the structure of the CMZ. Nuclear spirals are common in external galaxies, arise

frequently in simulations, and are consistent with the larger scale flow in and around the bar.

Although our model is not tuned to the CMZ, it does nevertheless successfully reproduce many aspects of the data. We have shown that the ridges and clouds seen in the data can be understood as the projection of the spiral arms and the shocks to the  $(l, v)$  plane. In particular, the main findings of this paper are as follows:

- (i) The two spiral arms produce two parallel ridges in the  $(l, v)$  plot, running diagonally from positive  $(l, v)$  to negative  $(l, v)$ .
- (ii) In the region where, in our interpretation, the shock connects to the  $x_2$  disc, cloud–cloud collisions are expected, both between material detaching from the spiral arms and between material running down the shock into the nuclear disc. Large cloud complexes with complex line-of-sight velocity structure, such as Sgr B2 and 1 $\frac{1}{2}$ 3, are examples of the result of such collisions from material detaching from the red arm and shocked material reaching the inner disc.
- (iii) It is possible for cloudlets and spurs of material to detach from the spiral arms as a consequence of the fact that streamlines have a component of the velocity perpendicular to the spiral arms. We interpret the polar arm and the dust ridge as an example of such a spur.
- (iv) A bead of material moving down the positive-latitude shock would produce a vertical emission feature at positive  $l$ , disconnected from the CMZ, similar to Bania Clump 2.
- (v) The compression produced by spiral shocks in the CMZ provides a natural mechanism for producing the densities and pressure necessary for the production of the molecular species that we observe in the region.

We have found that we can also capture the vertical structure [i.e. in the  $(l, b)$  plane] of the emission if we model the CMZ as a razor-thin disc whose axis is tilted by  $5^\circ$  with respect to the axis of the Galaxy at large. This fits with previous findings, but the dynamical reasons for the tilt remain unknown.

Moreover, we find that the wiggle instability, often seen in simulations of gas flow in barred potentials, may provide a natural explanation for two important CMZ facts:

- (i) The observed asymmetry of emission: Some particular signatures of unsteady flow are present in both the simulation and the data.
- (ii) The low star formation rate observed in the CMZ: The wiggle instability would provide the source of turbulence needed to suppress star formation.

The features of the model presented here are a qualitatively good match to the data, but there are a number of discrepancies, notably the too small line-of-sight velocities produced by nuclear spirals in the  $(l, v)$  plane. The model is by no means a ‘best fit’, and has been chosen to show that a simple gas flow model in a realistic potential can provide a useful and physically appealing interpretation of the features observed in the CMZ.

Directions for future work include the following:

- (i) Improving the fit by changing parameters of the underlying potential (e.g. the bar size, pattern speed, etc.) or the gas flow (e.g. the sound speed of the gas).
- (ii) Using simulations that include live chemical networks to test the hypotheses regarding (a) the origin of the asymmetry, and (b) the origin of vertical features such as Bania Clump 2. Such simulations are underway.

## ACKNOWLEDGEMENTS

The authors thank James Binney, Simon Glover, Diederik Kruijssen and the referee Mark Wilkinson for insightful comments and suggestions, and Jonathan Henshaw and Steve Longmore for stimulating discussions and for kindly providing the  $\text{NH}_3$  data. MR and JM acknowledge support from European Research Council (ERC) grant number 321067. MCS and RSK acknowledge support from the Deutsche Forschungsgemeinschaft in the Collaborative Research Centre (SFB 881) ‘The Milky Way System’ (subprojects B1, B2, and B8) and in the Priority Programme SPP 1573 ‘Physics of the Interstellar Medium’ (grant numbers KL 1358/18.1, KL 1358/19.2). RSK further thanks the European Research Council for funding in the ERC Advanced Grant STARLIGHT (project number 339177).

## REFERENCES

- Ann H. B., Thakur P., 2005, *ApJ*, 620, 197  
 Athanassoula E., 1992, *MNRAS*, 259, 345  
 Bally J., Stark A. A., Wilson R. W., Henkel C., 1988, *ApJ*, 324, 223  
 Bally J. et al., 2010, *ApJ*, 721, 137  
 Battersby C. et al., 2016, *Proc. IAU Symp.* 322, The Multi-Messenger Astrophysics of the Galactic Centre. Kluwer, Dordrecht, p. 90  
 Bertram E., Glover S. C. O., Clark P. C., Klessen R. S., 2015, *MNRAS*, 451, 3679  
 Binney J., Merrifield M., 1998, *Galactic Astronomy*. Princeton Univ. Press, Princeton, NJ  
 Binney J., Gerhard O. E., Stark A. A., Bally J., Uchida K. I., 1991, *MNRAS*, 252, 210  
 Bissantz N., Gerhard O., 2002, *MNRAS*, 330, 591  
 Bland-Hawthorn J., Gerhard O., 2016, *ARA&A*, 54, 529  
 Blitz L., Spergel D. N., 1991, *ApJ*, 379, 631  
 Burton W. B., Liszt H. S., 1978, *ApJ*, 225, 815  
 Burton W. B., Elmegreen B. G., Genzel R. eds., 1992, *The Galactic Interstellar Medium*. Springer-Verlag, Berlin  
 Contopoulos G., Papayannopoulos T., 1980, *A&A*, 92, 33  
 Cowie L. L., 1980, *ApJ*, 236, 868  
 Crocker R. M., Jones D. I., Melia F., Ott J., Protheroe R. J., 2010, *Nature*, 463, 65  
 Dickey J. M., Lockman F. J., 1990, *ARA&A*, 28, 215  
 Dobbs C. L., Glover S. C. O., Clark P. C., Klessen R. S., 2008, *MNRAS*, 389, 1097  
 Ferrière K., Gillard W., Jean P., 2007, *A&A*, 467, 611  
 Fragkoudi F., Athanassoula E., Bosma A., 2017, *MNRAS*, 466, 474  
 Fux R., 1999, *A&A*, 345, 787  
 Gilmore G., Reid N., 1983, *MNRAS*, 202, 1025  
 Heiligman G. M., 1987, *ApJ*, 314, 747  
 Henshaw J. D. et al., 2016a, *MNRAS*, 457, 2675  
 Henshaw J. D., Longmore S. N., Kruijssen J. M. D., 2016b, *MNRAS*, 463, L122  
 Jenkins A., Binney J., 1994, *MNRAS*, 270, 703  
 Kennicutt R. C., Jr, 1998, *ARA&A*, 36, 189  
 Kim W.-T., Seo W.-Y., Stone J. M., Yoon D., Teuben P. J., 2012, *ApJ*, 747, 60  
 Kim W.-T., Kim Y., Kim J.-G., 2014, *ApJ*, 789, 68  
 Kruijssen J. M. D., Longmore S. N., Elmegreen B. G., Murray N., Bally J., Testi L., Kennicutt R. C., 2014, *MNRAS*, 440, 3370  
 Kruijssen J. M. D., Dale J. E., Longmore S. N., 2015, *MNRAS*, 447, 1059  
 Kuno N., Nakanishi K., Sorai K., Shibatsuka T., 2008, *PASJ*, 60, 475  
 Langer W. D., Velusamy T., Morris M. R., Goldsmith P. F., Pineda J. L., 2017, *A&A*, 599, 136  
 Launhardt R., Zylka R., Mezger P. G., 2002, *A&A*, 384, 112  
 Leroy A. K. et al., 2009, *AJ*, 137, 4670  
 Li Z., Shen J., Kim W.-T., 2015, *ApJ*, 806, 150  
 Li Z., Gerhard O., Shen J., Portail M., Wegg C., 2016, *ApJ*, 824, 13

- Lindqvist M., Habing H. J., Winnberg A., 1992, *A&A*, 259, 118
- Lis D. C., Menten K. M., 1998, *ApJ*, 507, 794
- Liszt H. S., Burton W. B., 1978, *ApJ*, 226, 790
- Liszt H. S., Burton W. B., 1980, *ApJ*, 236, 779
- Longmore S. N. et al., 2012, *ApJ*, 746, 117
- Longmore S. N. et al., 2013a, *MNRAS*, 429, 987
- Longmore S. N. et al., 2013b, *MNRAS*, 433, L15
- Longmore S. N. et al., 2017, preprint ([arXiv:e-prints](https://arxiv.org/abs/1708.01526))
- McGinn M. T., Sellgren K., Becklin E. E., Hall D. N. B., 1989, *ApJ*, 338, 824
- McMillan P. J., 2017, *MNRAS*, 465, 76
- Martini P., Regan M. W., Mulchaey J. S., Pogge R. W., 2003a, *ApJS*, 146, 353
- Martini P., Regan M. W., Mulchaey J. S., Pogge R. W., 2003b, *ApJ*, 589, 774
- Molinari S. et al., 2011, *ApJ*, 735, L33
- Nagayama T., Omodaka T., Handa T., Iahak H. B. H., Sawada T., Miyaji T., Koyama Y., 2007, *PASJ*, 59, 869
- Navarro J. F., Frenk C. S., White S. D. M., 1996, *ApJ*, 462, 563
- Oka T., Nagai M., Kamegai K., Tanaka K., Kuboi N., 2007, *PASJ*, 59, 15
- Purcell C. R. et al., 2012, *MNRAS*, 426, 1972
- Rathborne J. M. et al., 2015, *ApJ*, 802, 125
- Reid M. J., Menten K. M., Zheng X. W., Brunthaler A., Xu Y., 2009, *ApJ*, 705, 1548
- Roberts W. W., 1969, *ApJ*, 158, 123
- Rodriguez-Fernandez N. J., Combes F., 2008, *A&A*, 489, 115
- Rodriguez-Fernandez N. J., Combes F., Martin-Pintado J., Wilson T. L., Apponi A., 2006, *A&A*, 455, 963
- Sawada T., Hasegawa T., Handa T., Cohen R. J., 2004, *MNRAS*, 349, 1167
- Schinnerer E., Maciejewski W., Scoville N., Moustakas L. A., 2002, *ApJ*, 575, 826
- Smith R. J., Glover S. C. O., Clark P. C., Klessen R. S., Springel V., 2014, *MNRAS*, 441, 1628
- Sofue Y., 1995, *PASJ*, 47, 527
- Sormani M. C., Binney J., Magorrian J., 2015a, *MNRAS*, 449, 2421 (SBM15a)
- Sormani M. C., Binney J., Magorrian J., 2015b, *MNRAS*, 451, 3437
- Sormani M. C., Binney J., Magorrian J., 2015c, *MNRAS*, 454, 1818
- Stark A. A., Bania T. M., 1986, *ApJ*, 306, L17
- van Albada G. D., van Leer B., Roberts W. W., Jr, 1982, *A&A*, 108, 76
- van de Ven G., Fathi K., 2010, *ApJ*, 723, 767
- Wada K., Koda J., 2004, *MNRAS*, 349, 270
- Walsh A. J. et al., 2011, *MNRAS*, 416, 1764
- Walter F., Brinks E., de Blok W. J. G., Bigiel F., Kennicutt R. C., Jr, Thornley M. D., Leroy A., 2008, *AJ*, 136, 2563
- Wegg C., Gerhard O., 2013, *MNRAS*, 435, 1874
- Weiner B. J., Sellwood J. A., 1999, *ApJ*, 524, 112

This paper has been typeset from a  $\text{\LaTeX}$  file prepared by the author.